Quantitative SEM characterisation of ceramic target *prior* and *after* magnetron sputtering: a case study of aluminium zinc oxide

ALI REZA JAHANGIRI*,†,‡,§ [iD], PAYAM RAJABI KALVANI†,‡,§ [iD], SAMANEH SHAPOURI†,‡,§ [iD], AMIRHOSSEIN SARI†,‡ [iD], ŞTEFAN ŢĂLU‖ [iD] & YOUSEF SEYED JALILI†,‡,§

*NanoLund, Lund University, Box 118, 22100 Lund, Sweden

†Department of Physics, Faculty of Science, Science and Research Branch, Islamic Azad University, Tehran, Iran

‡Plasma Physics Research Centre, Science and Research Branch, Islamic Azad University, Tehran, Iran

§Nano-Optoelectronics Laboratory, Sheykh Bahaee Research Complex, Science and Research Branch, Islamic Azad University, Tehran, Iran

‖The Directorate of Research, Development and Innovation Management (DMCDI), Technical University of Cluj-Napoca, Cluj-Napoca, Cluj, Romania

Summary

Till now electron microscopy techniques have not been used to evaluate the plasma–target interactions undergone during the magnetron sputtering process. The destructive nature of this interaction severely alters the target microstructure. Utilising quantitative microscopy techniques can shed light on the complex plasma and solid-state processes involved which can ultimately lead to improved functional thin film deposition. As a representative functional material, aluminium-doped-zinc oxide (AZO) is an upcoming alternative to conventional transparent electrode wherein the process optimisation is of great importance. In this paper, we evaluate the pre- and post-sputter field emission scanning electron microscopy (FESEM) data for ceramic AZO target fabricated at three final sintering temperatures (1100°C, 1200°C and 1300°C). In all cases, grain boundaries are merged in addition to a visible reduction in the secondary phases which makes segmentation-based image analysis challenging. Through surface statistics (i.e. fractal dimension, autocorrelation length, texture aspect ratio and entropy) as a function of magnification we can quantify the electron microscopy image of the microstructure. We show that the plasma–microstructure interaction leads to an increase in autocorrelation length, texture aspect ratio and entropy for the optimum AZO ceramic sputtering target sintered at 1200°C. Furthermore, a maximum reduction in fractal dimension span (as determined by exponential regression) is also observed for 1200°C. In addition to the evaluation of plasma effects on sintering, our approach can provide a window towards understanding the underlying thin film

growth mechanisms. We believe that this technique can be applied to the defect characterisation of a wide range of polycrystalline ceramic sputtering targets (e.g. ITO, CZTS, GAZO and so on) with the ultimate goal of improving the magnetron sputtering process and the resulting functional thin film.

Introduction

Within the realm of materials science, electron microscopy is commonplace for micromorphology evaluation; which is inaccessible to traditional diffraction limited optical microscopy. An effective microscopic acquisition and analysis is of significant importance in the study of functional ceramics in which the sintering process can be probed through scanning electron microscopy (SEM). The SEM data acts as a launching pad for a phenomenological understanding of grain growth and hence functional properties. Eventually, the insight acquired can be directed towards optimising the fabrication process (Joly-Pottuz *et al.*, 2011; Sun *et al.*, 2020). Although scanning probe microscopy (SPM) techniques can potentially provide the real height and with high lateral resolution, it is critical to use a sharp and narrow tip. Techniques have been developed for producing tips satisfying this criteria, yet erosion and corrosion will inevitably lead to tip damage during use (Knápek *et al.*, 2017). Furthermore, electron microscopy has been able to obtain high quality real-time images for over four decades (Barber & Emerson, 1979) whereas video SPM is a recent novelty.

In line with this, SEM-based techniques are commonly applied to characterise newly discovered materials, as well as to investigate the effect of initial precursors and processing/environmental conditions. For example, Mortazavi *et al.* (2020) use SEM images acquired prior to and after plasma polymerisation (for 5 and 10 min) of biaxially oriented

Correspondence to: A. R. Jahangiri, NanoLund, Lund University, Box 118, 22100 Lund, Sweden. Tel: +46 (0)46 222 00 00; e-mail: al6687ja-s@student.lu.se, alireza.jahangiri@srbiau.ac.ir

polypropylene (BOPP) to provide a rational for particle growth. Odziomek have demonstrated a series of image filtering, thresholding and segmentation procedures on SEM images to automatically extract nanoparticle descriptors including perimeter, area and circularity (Odziomek *et al.*, 2017). Reyes-Gasca & Becerril (2019) made use of electron microscopy for studying how the morphology of human molar changes when heating up to 1000°C. In fact, some studies have incorporated a heater within the SEM chamber (HT-SEM), allowing for in situ imaging of the sintering process, although the behaviour is slightly different compared to normally sintered ceramics (Joly-Pottuz *et al.*, 2011; Podor *et al.*, 2019).

While traditional analysis of SEM is based on visual or limited masked based analysis, there is a growing body of literature quantitatively exploring the data through machine vision (Yan *et al.*, 2019) and surface statistics (Țălu *et al.*, 2016a,b; Klapetek, 2018). Roding *et al.* (2016) demonstrated that a silica ceramic fabricated via spark plasma sintering undergoes anisotropic grain growth. Mozaffari *et al.* (2020) demonstrated that after CO adsorption, higher fractal dimensions (as determined via FESEM) are correlated with enhanced functionality as a result of altered gas-microstructure interactions. Significant morphological variations are observed upon ion beam implantation of copper oxide thin films, that are reflected in the surface statistics as well (Jafari *et al.*, 2020). Shakoury *et al.* (2020) and Monemdjou *et al.* (2014) demonstrated a correspondence between fractal analysis and optical properties for magnetron sputterewd zinc sulfide (ZnS) and aluminium-doped zinc oxide (AZO) thin films, respectively. Since the micromorphology of material with competing phases can provide insight into the chemical and crystal defects (Țălu *et al.*, 2018; Papež *et al.*, 2020; Rajabi Kalvani *et al.*, 2020), electron microscopy can be a valuable yet accessible tool for the assessment of functional parameters as seen in the aforementioned studies. While many methods for defect characterisation exist, the semiconductor industry is in need of a facile and accessible approach for analysis of optoelectronic devices during and after the fabrication process (Papež *et al.*, 2020).

Although some research has been done on the analysis of sputtered thin films, the alteration of the target microstructure as a result of the sputtering process has been severely overlooked. It is well known that the destructive plasma–microstructure interactions occurring on the surface of the target can lead to a 'racetrack' phenomenon which is clearly visible to the naked eye (Nakano *et al.*, 2015; Wu *et al.*, 2019). Furthermore, experimental studies have shown that during plasma-enhanced chemical vapour deposition, the resulting product morphology is greatly influenced by the plasma parameters (e.g. electron temperature) (Kudryashov *et al.*, 2019).

A wide range of interacting factors influence magnetron deposition of thin films. These include gas composition (Bose *et al.*, 2018; Țălu *et al.*, 2018), flow rate/pressure (Ma *et al.*, 2019; Lee *et al.*, 2020; Shakoury *et al.*, 2020), deposition time (Dallaeva *et al.*, 2012; Ma *et al.*, 2019; Lee *et al.*, 2020), deposition rate (Taheriniya *et al.*, 2018), power (Ma *et al.*, 2019; Lee *et al.*, 2020), distance of substrate from target (Sangwaranatee *et al.*, 2018), substrate temperature (C. Taheriniya *et al.*, 2018; Ma *et al.*, 2019; Rajabi Kalvani *et al.*, 2019) and the target fabrication process (Wu *et al.*, 2012, 2019; Liu *et al.*, 2020). Since the target itself is one of the key factors contributing to the microstructure of the substrate, the evaluation of plasma–microstructure is key to not only better understanding the process but also to allow for optimisation (Dallaeva *et al.*, 2012; Wu *et al.*, 2019; Chen *et al.*, 2020). When competing phases occur, secondary phases may emerge leading to various effects such as Zener pinning that ultimately affect the local chemical reactivity (Huang *et al.*, 2018; Thiruvalluvan *et al.*, 2018). Additionally, we have previously shown that the aluminium sputter conditions can alter the micromorphology of the anodised alumina (Taheriniya *et al.*, 2018). Several studies have shown obstructions (e.g. sputtering target) can lead to unique variations in the electron transport as well as the momentum transfer of fast neutral (heavy) particles in low-pressure plasma, especially when subject to a magnetic field wherein charge exchange may play a significant role (Fukao *et al.*, 2000; Sari *et al.*, 2004, 2008; Donkó *et al.*, 2007). Spatial plasma diagnostics methods – such as Langmuir probes (Raggl *et al.*, 2017; Sagás *et al.*, 2018) – are complex and often invasive, which perturbate the plasma environment in the process leading to loss in data accuracy and reliability. In this study, we will adapt the electron microscopy methods traditionally used on the sputtered thin film to investigate the surface micromorphology of the ceramic sputtering target prior to and after inducing the plasma.

Previously, we have demonstrated a novel economic multi-step sintering method to fabricate the initial AZO target (Rajabi Kalvani *et al.*, 2020) which was then installed in the sputtering chamber and utilised for the production of thin films (Rajabi Kalvani *et al.*, 2019). Submicron zinc oxide together with nanometric alumina powder was used which resulted in the formation of exsolution and recrystallisation effects on the presputtered target. In this study, we will delve deeper into a comparison of pre- and postsputter micromorphology to obtain a phenomenological understanding of the magnetron sputtering process, as observed by the target microstructure.

Materials and methods

Fabrication of AZO ceramic sputtering target

Aluminium-doped zinc oxide ceramic sputtering target consisting of 98% w/w ZnO submicron precursor with 2% w/w Al_2O_3 nanopowder ($\sim$80 nm) has been fabricated via multi-step pressureless sintering at 1100°C, 1200°C and 1300°C, as detailed in our previous work (Rajabi Kalvani *et al.*, 2020).

Magnetron sputtering method

All targets have been part of the magnetron sputtering target as described in (Rajabi Kalvani *et al.*, 2019). Briefly, magnetron sputtering involving has been performed with a nominal operation pressure of 5×10^{-3} torr after the introduction of high purity argon gas to a chamber pressure of 10^{-6} torr. A power of 150 W was applied, with a radio frequency source corresponding to 13.56 MHz (ISM Band Type B) for 1 hour.

Image processing and quantitative analysis

Analysis of the microstructure was performed using a FE-SEM apparatus (Hitachi S-4160 Japan) with an acceleration voltage of 20 kV. Images have been acquired at various magnifications.

Fundamentally, it is not possible to use standard grain-based statistics to evaluate the postsputter microstructure due to the grain boundaries being barely visible. Thus, other statistics such as autocorrelation function, texture aspect ratio, fractal dimension and entropy are applied. All image processing has been performed in the open source Gwyddion software package (Nečas & Klapetek, 2012; Klapetek, 2018).

Several quantitative metrics are utilised based on the analysis of the FESEM images acquired pre- and postsputter from the magneton sputtering target.

The use of fractal dimension (Shanmugavadivu & Sivakumar, 2012; Ţălu, 2012) and autocorrelation length (Rockstuhl *et al.*, 2010) postsputter can provide an additional metric that will help identification and optimisation of the subsequent thin film production, especially with regards to optimum addition of nanopowder dopant to the green compact.

The autocorrelation function provides a quantitative measure of the convolution of an image with itself and can be defined for an image as a 2D (two-dimensional) matrix with the following relation (Robertson, 2012):

$$G_{ii}(a.b) = \sum_{x}^{M} \sum_{y}^{N} i(x.y) * i(x - a.y - b).$$ (1)

where $G_{ii}(a,b)$ is the autocorrelation function in real space; $i(x,y)$ denotes the image intensity at location (x,y) for the values a and b corresponding for the distance/lag from the specified position.

In this study, the normalised radial average value is computed. Upon applying the function to an image, the result is another image. The value upon which the autocorrelation length decays to 0.2 is denoted as the autocorrelation length, S_{al}.

Since the autocorrelation length (S_{al}) does not directly convey information about the (an)isotropic properties of the surface, the texture aspect ratio (S_{tr}) parameter was computed (Ţălu *et al.*, 2016a,b; Shapouri *et al.*, 2018) with the following relation (Nečas & Klapetek, 2012):

$$S_{tr} = \frac{\text{Maximum } S_{al}}{\text{Minimum } S_{al}}.$$ (2)

The Shannon entropy of images was determined according to a simple histogram approximation (Shannon, 1948; Purwani *et al.*, 2017; Klapetek, 2018):

$$S \approx -\sum_{i=1}^{n} p_i \log \frac{p_i}{w_i},$$ (3)

where p_i and w_i denote the pseudo-height value and width of the ith histogram bin respectively. Apart for an ideal normal distribution, the calculated entropy value is dependent on the bin width. Thus, the entropy is estimated over a wide range of bin width and the inflection point is chosen as the bin width.

Furthermore, to obtain insights into the self-similarity and complexity of digital images (for quantitative analysis of the postsputter images with merged grain boundaries), the fractal dimension was computed.

For a bounded set $F \subset R^n$ (Euclidean n-space), the set F is said to be self-similar when F is union of N_r distinct nonoverlapping copies of itself, each of which is similar to F scaled down by a ratio r. Fractal dimension D of F (computed as the box-counting dimension) can be calculated according the following relation (Shanmugavadivu & Sivakumar, 2012; Ţălu, 2015):

$$D = \lim_{r \to 0} \frac{\log (N_r)}{\log (1/r)}.$$ (4)

Braun *et al.* (2018) showed that grain boundaries exhibit a fractal property and this property can provide insights towards grain boundary migration for optimising the material properties. The interested Reader is guided to a paper by Mitic *et al.* (2019) on the importance of fractal analysis for numerical modelling and practical realisation of functional ceramics published in *Ceramics International*.

Results and discussion

FESEM images analysis

A visual comparison of the FESEM images is shown in Figure 1.

An obvious difference can be observed visually between the presputter images which highlights the fabrication and presputter properties. Briefly, we have previously shown that for the presputter microstructure the grain size of the main phase increases with higher temperature, but so does the secondary phase. A highly porous structure is observed for 1100°C for both pre- and post-sputter conditions (Fig. 1A), which can translate into less desired functional properties such as lower density and higher resistivity. Furthermore, the Gaussian distribution of the secondary phase particles widens
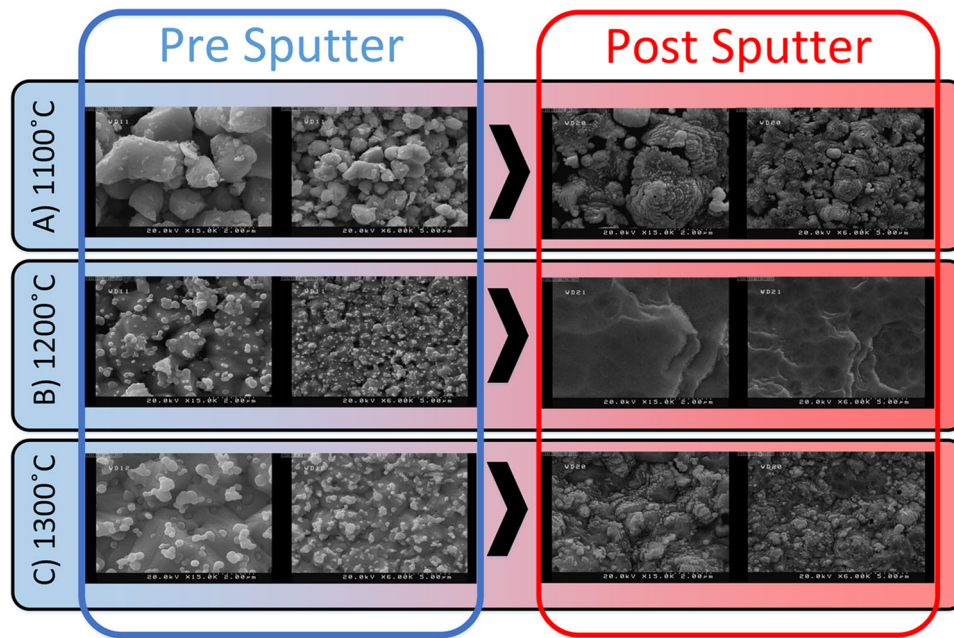
Fig. 1. Visual comparison between pre- and postsputtered FESEM images for AZO (aluminium-doped zinc oxide) ceramic targets sintered at: (A) 1100°C, (B) 1200°C and (C) 1300°C.

considerably at 1300°C, which hints at possible competing recrystallisation-exsolution mechanisms that can signal uneven atomic distribution of aluminium in the main phase (Rajabi Kalvani *et al.*, 2020). However, the variation in the postsputter images is less subtle. It can be visually observed that for the postsputter target sintered at 1200°C (Fig. 1B), the appearance seems more homogenous with less secondary phase particles. Analysis of the postsputter microstructure will allow for the optimal duration of the shutter operation such that minimal time is required thus reducing material and time waste. Also, we suggest that the postsputter is analysed for the quantitative evaluation of what constitutes a 'good' target since in practice the postsputter target is mapped to the substrate and *not* the presputter microstructure.

As seen in Figure 1, these secondary phases are mostly observed on the grain boundaries, which suggest that the Zener pinning mechanism is still present even after sputtering. Similar micromorphological structures have been observed in polished and unpolished FESEM micrographs of AZO ceramic targets by Liu *et al.* (2020). In particular, while sintering at 1100°C (Fig. 1A) and 1300°C (Fig. 1C) results in observable secondary phases in the postsputter FESEM images, it is nearly nonexistent for the AZO target sintered at 1200°C (Fig. 1B). This can hint towards the more homogenous distribution of Al atoms within the target and thus possibly improved sputtering characteristics. As the calling card of Zener pinning, it can be deduced that the severe reduction in secondary phases signals a more homogenous grain distribution, which can be confirmed in the presputter grain size analysis as seen in

Figure 1 (according to the results obtained in Rajabi Kalvani *et al.*, 2020). It would be expected that based on this factor alone, the morphological characteristics would be profoundly different, though electrical characteristics are dependent on other factors as well. The secondary phase at 1200°C for both pre- and postsputter has a spherical shape, which suggests that the growth is governed by a lowering of the surface energy (Zhao *et al.*, 2014).

In addition, the smaller size of the postsputtering spinel phase as seen in high-zoom images shown in Figure 2(A) can be attributed to the collision of the energetic incident argon particles. These images were obtained by automatic grain thresholding performed with the watershed algorithm, applying a filtration of grains under 20 pixels and a 3 pixels grow and 2 pixels shrink Euclidian operator, with merging prevention. This evolution of the secondary phase precipitates hints towards a complex driving force resulting from changes in interfacial energy. In itself, this may also be an indicator of tension and stress in the microscale (Chen *et al.*, 2003).

The existence of a secondary phase with varying dimensions and aggregations (Rajabi Kalvani *et al.*, 2020) is a clear indicator of unstable growth kinetics and, ultimately, recrystallisation and reabsorption into the main phase. However, additional exsolution may also occur: recrystallisation-exsolution is a two-way street (Huang *et al.*, 2018). Studies have shown that aluminium atoms may undergo electromigration which can be a possible source of perturbation in the polycrystalline structure resulting in the alteration of secondary phase precipitates (Ma & Suo, 1993) that can in turn
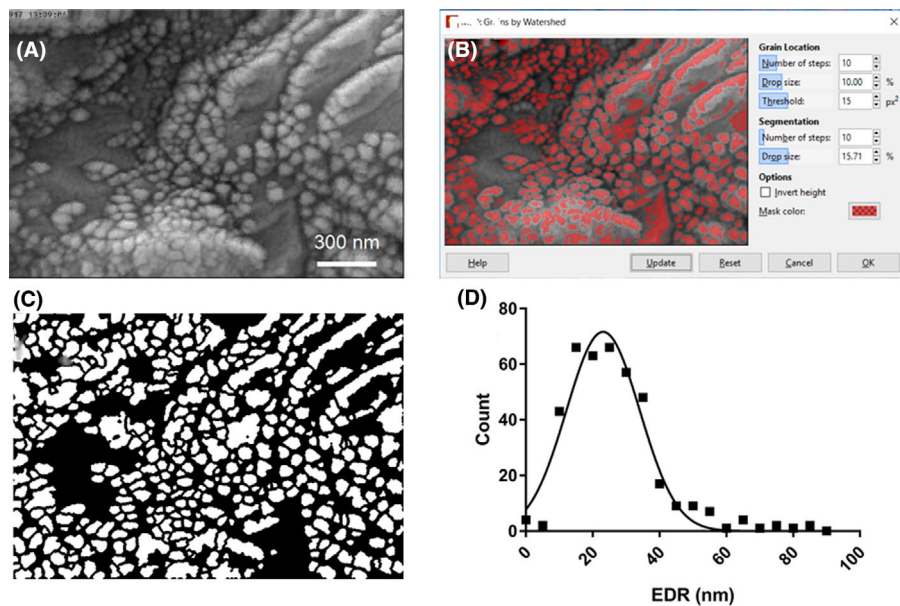
Fig. 2. (A) High magnification (×60k) of postsputtered AZO (aluminium-doped zinc oxide) ceramic target sintered at 1100°C, upon which (B) Watershed algorithm is applied which results in a (C) binary mask. (D) The distribution of the secondary phase particles.

manifest itself in the form of morphology, chemical and/or crystal variations. It is well known that high-energy radiation can alter the functional properties of semiconductor devices, which is a serious concern in space-based solar power (Pelton, 2019; Papež *et al.*, 2020). Further studies are needed to quantify the relation between incident particle collision energy and postsputter secondary phase micromorphology.

It can be said that upon postsputtering, two key sintering mechanisms (dominated by heat and electricity) lead to a polycrystalline solid. Upon the contact of two grains of different sizes, the smaller grain is 'gobbled up' (consumed) by the larger grain. Grain rotation is required, which requires a large input of energy. This merging leads to the eventual loss of grain boundary (Castro & Benthem, 2013). An additional factor for the indiscriminate grain boundaries can be attributed to the intense sputtering of high-energy atoms from the surface of the target, as well as interaction with high-energy Ar atoms present in the sputtering chamber.

Ceramic sintering is traditionally evaluated via the study of the grain size. However, as evident in Figure 1, this approach is not suitable for evaluating the postsputter images. We can see that the postsputter FESEM images demonstrate a merger of grain boundaries. Relying solely on the presputter data to evaluate the postsputter results (both in the target and the sputtered thin film) will only give a partial picture especially since it is the convolution between the complex and turbulent (both on an atomic and macro scale) plasma–ceramic interaction that will ultimately determine the outcome of both the sputtering target microstructure as well as the functional characteristics of the as-deposited thin film. After sputtering, we can see clear morphological differences. The grain boundaries are

indistinguishable. This can be attributed to the fact that sputtering power leads to a 'spark plasma sintering'-like treatment within the sputtering chamber, leading to a more homogeneous layer (Kudryashov *et al.*, 2019; Chen *et al.*, 2020). Based on a statistical analysis of the pre- and post-sputter images we will demonstrate that the secondary phase particles are effectively suppressed by the plasma in 1200°C, whereas they are still evident in the 1300°C target.

Autocorrelation analysis

Autocorrelation provides a metric for self-similarity between the image and a spatially delayed version of itself. The autocorrelation length has been graphical displayed in Figure 3. It can be seen that as the magnification increases, the autocorrelation length decreases. Thus, an inverse relationship exists between magnification and autocorrelation length for both pre- and post-sputter conditions. This can be attributed to the greater resolution of finer features within the sample. However, the general trend follows an exponential decay.

For 1200°C and 1300°C, the span of the fitted exponential decay function is considerably higher for the postsputter compared to the presputtered autocorrelation analysis. That is, the autocorrelation length is not very dependent on the magnification prior to sputtering, yet the surface features clearly become more magnification dependent upon sputtering. This is particularly observable for 1200°C. On the other hand, the half-life is shifted to lower magnifications for the postsputter analysis. This suggests that more variation is observed for the microstructure at lower magnifications. The higher initial autocorrelation length for the presputter FESEM of the sample
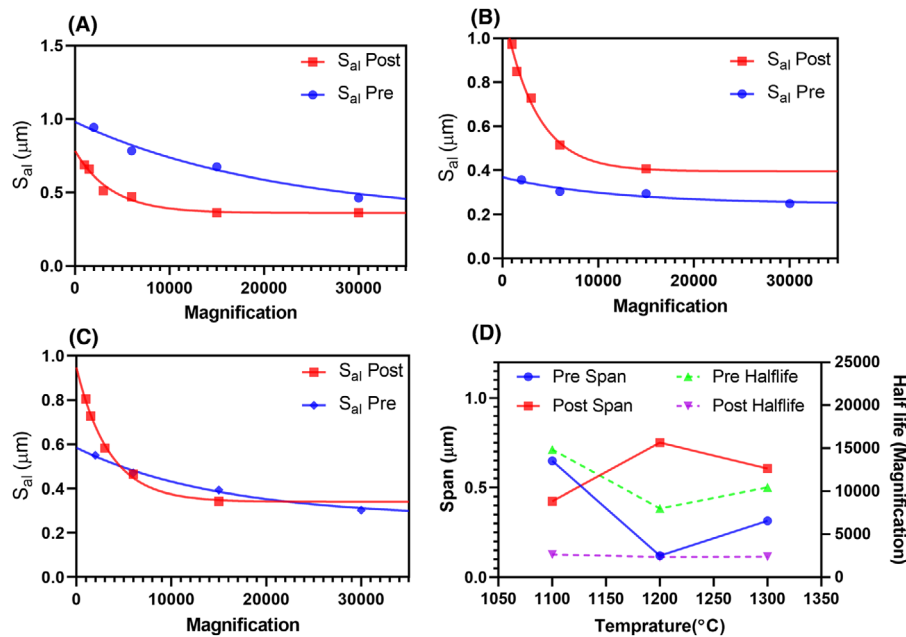
Fig. 3. Autocorrelation analysis of FESEM for pre- and postsputtered AZO (aluminium-doped zinc oxide) ceramic targets at: (A) 1100°C, (B) 1200°C and (C) 1300°C. (D) A comparison of fitted exponential function.

sintered at 1100°C can be attributed to the existence of pores, which increases the 'lag' of the signal (Heilbronner, 1992; Lee *et al.*, 2017). Based on the higher variation of the span values (as well as the noticeably higher plateau) it is clear that the sputtering process has shown a higher interaction with the target sintered at 1200°C. It is interesting to emphasise that the secondary phase particles have been eradicated in the postsputter target sintered at 1200°C, which may explain the strong variations in the span. Yet since this change in the span is observed overall targets, it is plausible that the magnetron sputtering plasma inflicts scale dependant anisotropic erosion in the ceramic target. Contrary to common belief, the electron density during deposition is highly spatially and temporally variant. On the other hand, Panjan & Anders (2017) experimentally demonstrate that an electric double layer energises drifting electrons. Prior to transporting across the double layer, they are at the lowest energy level yet after crossing the double layer they are at highest potential. It must be noted that the double layer is asymmetric and a large imbalance of charge is observed.

Taking into account the recrystallisation capabilities of the sputtering plasma (which can provide the additional energy required to reincorporate the secondary phase into the main phase), the autocorrelation length at 1300°C shows little increase which may be indicative of the inability of the sputtering conditions to alter the surface features, namely the secondary phase particles as observed in Figure 1(C). Thus, higher sintering temperature does not always lead to a more desirable surface microstructure. This is important towards obtaining a high-quality target since the secondary phase par-

ticles signal uneven distribution of dopants. This ultimately affects the functional characteristics of the sputtered thin film (Papež *et al.*, 2020). However, in the case of thermoelectric materials, this may in fact be a desired property (Ibáñez *et al.*, 2019).

Texture aspect ratio analysis

Analysis of the texture aspect ratio can provide a measure of (an)isotropicity, which can provide insight into the grain growth mechanisms during pressureless sintering as well as the effect of the complex plasma environment involving high electric fields in the presence of magnetic fields with high electron temperature.

Texture aspect ratio of FESEM for pre- and postsputtered AZO targets at various temperatures is shown in Figure 4.

Interestingly, the texture aspect ratio for the AZO target sintered at 1100°C shows significant variations in the presputter FESEM images (Fig. 4A). That is, the (an)isotropicity is a function of the magnification, as well as the spatial position of the acquired FESEM images as can be seen in the variation of texture aspect ratio shown in Figure 3(A). This can be an indicator of uncompleted densification as a result of the random orientation of grains, which can result in high crystal misorientations and thus high local variations in chemical potential. A similar issue can be observed in Figure 4(C), where the aspect ratio exhibits a quasi-linear relation with magnification. It is possible that this could be due to the secondary phase particles observed at the target sintered at 1300°C (Fig. 1C). Thus, prior to the *in situ* magnetron sputtering, it is vital to ensure
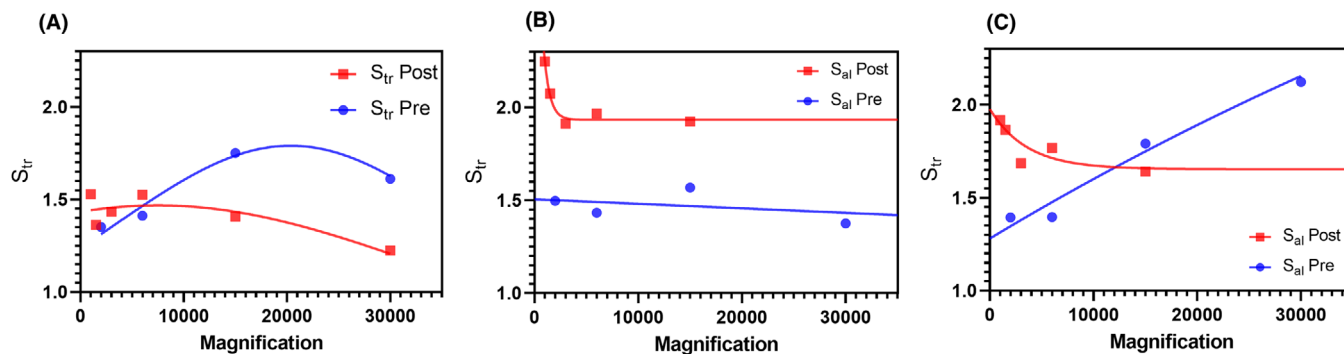
Fig. 4. Texture aspect ratio of FESEM for pre- and postsputtered AZO (aluminium-doped zinc oxide) ceramic targets at: (A) 1100°C, (B) 1200°C and (C) 1300°C.

that the required densification is achieved. Similar randomness is observed in the sample sintered at 1300°C, with the difference that the presputter texture aspect ratio is more chaotic rather than the postsputter regime. This can show that the *in situ* plasma sintering has shown to be effective, however, since the pressureless sintered target did not show the desired properties, it is possible that this is due to a dynamic equilibrium, which is knocked out of place by the plasma, leading to uneven sputtering of thin films by the target sintered at 1300°C. It must be emphasised that all the targets have been sputtered under similar sputtering conditions since the deposition conditions can affect the resulting surface characteristics (Ţălu *et al.*, 2018, 2019).

The texture aspect ratio for 1300°C also rises, but not as intense as 1100°C. On the other hand, sintering at 1100°C results in a steady decrease in the texture aspect ratio at higher magnification. It has been shown that not only does Zener pinning induce anisotropic grain migration, but the subsequent recrystallisation texture resulting from the reduction of the secondary phase (and hence the Zener drag force) is also orientation-dependent (Huang *et al.*, 2018). The ceramic target sintered at 1200°C (Fig. 4B) is unique. The presputter FESEM shows a quasi-uniform trend for the texture aspect ratio prior to sputtering. However, after sputtering, exponential decay is clearly visible. This may suggest that the erosion of atoms from the surface by the sputtering plasma has a preferred orientation, which is similar at all length scales. This, in turn, may reflect the scale of the variation in the local electromagnetic field on the sputtering target surface (Panjan & Anders, 2017). Furthermore, the plateau has also shown a large change. Similar to the results obtained for the autocorrelation analysis (Fig. 3B), there is a significant difference in the plateau for both the pre- and postsputter images. However, since the exponential decay was not able to fit the texture aspect ratio for 1100°C (Fig. 4A) and 1300°C (Fig. 4C), a quantitative comparison of the fitted function is not possible.

The 'aggregation' seen at lower magnification turns to distinguishable particles at higher magnification, thus increasing the complexity of the surface for the targets sintered at 1100°C and especially 1300°C. Upon the application of external energy and/or rapid change in material conditions a homogeneous resulting surface microstructure is observed which can be an indicator of diffusion-hindered aggregation phenomena (Ortega *et al.*, 2017; Jesus *et al.*, 2019).

As confirmed to NMR studies performed by Sun *et al.*, a small amount of aluminium doping within the wurtzite structure leads to a critical increase in the conductivity that is assumed to be related to the Knight shift whereas the emergence of secondary phases compromises this balance (Sun *et al.*, 2019). Furthermore, this change in the atomic arrangement leads to a presence in the microstructure (Sun *et al.*, 2020), confirming the link between surface characteristics and conductivity.

Traditionally, fabricating highly isotropic materials has been (and still is) a major goal (Vermolen *et al.*, 2009). However, an increasing body of research is focusing on appreciating the anisotropic nature of heterogenic materials which has opened up novel areas of research (Zhang *et al.*, 2019). Ibáñez *et al.* (2019) have exploited chemical/crystal anisotropicity to fabricate high figure of merit (FOM) thermoelectric energy conversion nanocomposites. Furthermore, Brown *et al.* (2017) demonstrated that the chemical self-propulsion of chemical swimmers (such as Janus microspheres) is dependent on the inherent symmetry-breaking structure of the bimetallic particle. Therefore, understanding the anisotropic surface characteristics has far-reaching consequences towards the quest for gaining a phenomenological understanding of various polyphase materials.

Entropy analysis

Entropy can provide a measure of the 'type' of image, allowing for categorisation based on acquisition parameters. Entropy is more sensitive to the magnification, rather than the data within the image. It is possible to use this to compare images obtained across various magnifications in the form of a magnification normalised figure of merit. In fact, a
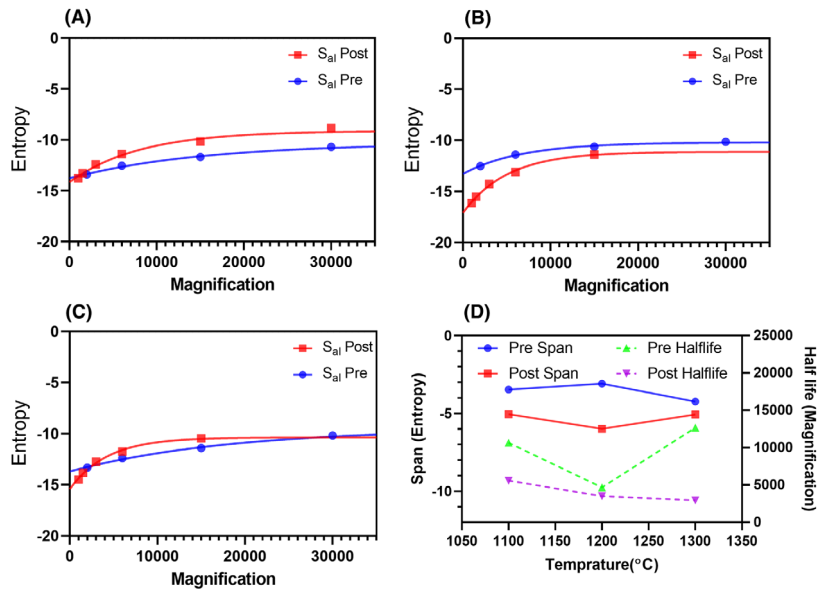
Fig. 5. Entropy of FESEM for pre- and postsputtered AZO (aluminium-doped zinc oxide) ceramic targets at: (A) 1100°C, (B) 1200°C and (C) 1300°C. (D) Comparison of fitted exponential function.

characteristic curve can be observed, which clearly fits an exponential decay. In stark contrast to the texture aspect ratio (Fig. 4), a very good fit is observed for all three samples, both pre- and postsputter.

Among all three temperatures, it is only for 1200°C (Fig. 5B) that we can see a reduction in entropy after sputtering. In fact, while the starting entropy for 1100°C (Fig. 5A) and 1300°C (Fig. 5C) is lower, the resulting entropy for 1200°C is lower than both of them. This shows that a reduction in the amount of data is observed in the images, which corresponds to the near-total elimination of secondary phase particles in a final sintering temperature of 1200°C (Fig. 1). Hence, not only does entropy provide a measure of the magnification, but it also provides a measure of the quality; since we observed that the sample sintered at 1200°C had the most desirable characteristics. Also, it is less sensitive to variation between the surface.

Also, since the secondary phase was not eliminated in the FESEM images for the target sintered at 1300°C, one would not expect much change in the magnification dependent entropy (Fig. 5C).

In general, the pre- and postspan values do not change significantly, even though a considerable change is observed for the pre- and postsputter entropy values as noted earlier for 1200°C. However, it is interesting to note that while the pre-half-life values are maximum for 1300°C, a linear downward trend with respect to temperature is observed. It would be interesting to see what the phenomenological basis of this is and if this could be used to identify the sintering temperature exclusively based on the postsputter FESEM images.

Fractal analysis

The cube counting method for fractal analysis was applied. The fractal dimension provides a measure of self-similarity within the structure, an essential metric that can provide insight into grain growth dynamics and the postsputter micromorphology (Ţălu, 2015).

Similar to the autocorrelation and entropy analysis, we can see that the fractal dimension clearly fits with an exponential decay function. Interestingly, the postsputter fractal dimension for has decreased the most which are in contrast with the results show in our AZO thin film study where we showed a high fractal dimension leads to a greater figure of merit (Rajabi Kalvani *et al.*, 2019).

The fractal dimension of FESEM for pre- and postsputtered AZO targets at various temperatures is shown in Figure 6.

The fractal dimension for the postsputter compared to the presputter of 1100°C (Fig. 6A) is considerably higher in comparison with both 1200°C (Fig. 6B) and 1300°C (Fig. 6C). This can be possibly attributed to the existence of pores, which have been shown to reduce the fractal dimension. While the fractal dimension for the presputter of 1200°C (Fig. 1B) and 1300°C (Fig. 1C) is similar, the postsputter situation is different. For 1200°C, not only has the fractal dimension reduced, but also the fractal dimension is less dependent upon magnification. This may suggest that the fractal features of the structure are scale independent and thus a more homogenous microstructure is achieved as part of the plasma–microstructure interaction (Kudryashov *et al.*, 2019). This is further verified by Figure 6(D) where the reductions both span and half-life in the postsputter FESEM images
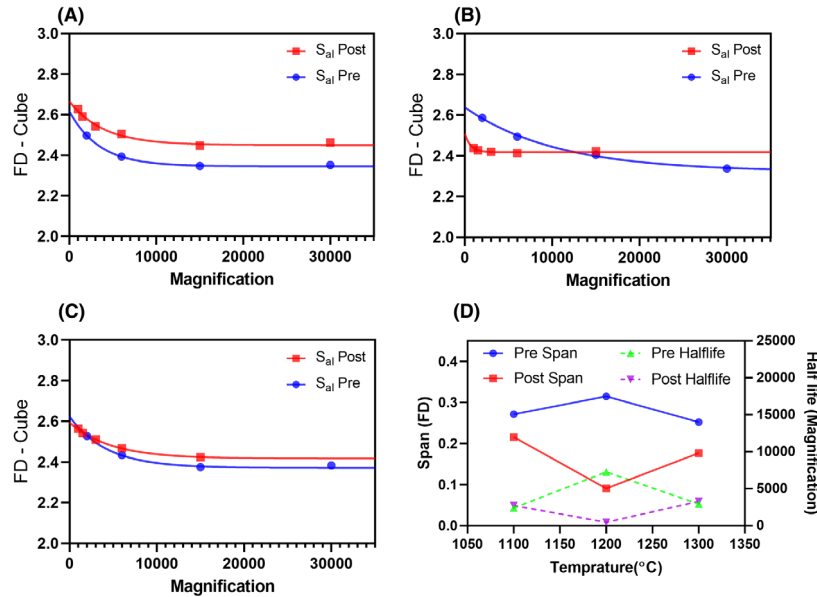
Fig. 6. Fractal dimension of FESEM for pre- and postsputtered AZO (aluminium-doped zinc oxide) ceramic targets at: (A) 1100°C, (B) 1200°C and (C) 1300°C. (D) Comparison of fitted exponential function.

are maximum. Furthermore, the 1200°C postsputter values are minimum. Interestingly, the values for half-life are not altered noticeably for 1100°C nor 1300°C.

Therefore, it could be deduced that as a result of plasma–microstructure interaction, the surface of the target sintered at 1200°C exhibits more homogeneous characteristics and thus results in optimum functional characteristics of the sputtered thin films. Namely, we can see that whereas the postsputter shows a polynomial trend for the 1300°C, this is more in the form of a straight line, showing little dependency on the magnification (Fig. 1D).

This may have been the reason for a more homogenous postsputter surface as demonstrated by the fractal dimension. Since fractal dimension is indifferent towards grain size and aggregates, it may be a better indicator as a figure of merit for improving product characteristics in surface response methodology studies (Risović & Pavlović, 2013; Mitic *et al.*, 2019). Recent studies have investigated the effect of fractal dimension of optoelectrical materials (van Veen *et al.*, 2017; Rajabi Kalvani *et al.*, 2019; Ţălu *et al.*, 2019), and may even lead to self-similar properties based on self-similar grain morphology (Tavakoli & Jalili, 2014; García-Cervantes *et al.*, 2017).

Conclusions

Magnetron sputtered functional thin film production is a plasma-driven corrosion process. Uneven plasma etching of the surface microstructure (manifesting intergranular corrosion) will lead to the rapid wear of the magnetron sputtering target as well as a loss in the functional properties of the fabricated thin film. Understanding the mechanisms at play will help towards advancing science and technology for more functional and economical thin films. Quantitative sputtering target surface evaluation demonstrated here provides a window into less observed experimental phenomenon.

In our case study of an aluminium-doped zinc oxide (AZO) target, we have shown that it is possible to investigate the effects of plasma–microstructure interaction through quantitative magnification dependent properties such as autocorrelation length (Fig. 3), texture aspect ratio (Fig. 4), entropy (Fig. 5) and fractal dimension (Fig. 6). In addition to eliminating surface contamination, this may be the reason why presputtering is generally used in magnetron sputtering in which grain merging similar to electrical field-assisted sintering is induced. We can conclude that a suitable sintering temperature (1200°C) leads to the following surface characteristics in the resulting target:

- Low-magnification dependency in the presputter and increase in postsputter for autocorrelation length and texture aspect ratio.
- Constant, magnification independent fractal dimension.
- Increase in entropy upon sputtering.

Future evaluations of the destructive plasma–microstructure intereactions for other transparent conducting oxides (TCO) such as indium tin oxide (ITO) and CZTS will open up a new window into the polyphase/polycrystalline ceramic fabrication process. Additionally, fundamental insight can be gained on how plasma interacts with a conducting target, which could possibly increase our understanding

of charge exchange, cold ions and secondary electrons. In particular, impurity segregation at the grain boundaries may provide additional insight into a phenomenological understanding of the optimum conditions for functional thin films, as well as defect evolution which plays a critical role in the semicondutor industry. The spatial defect characterisation will become even more important as spintronics and memeristors become mainstream technologies. Extracting the morphological variations as quantitative parameters (e.g. texture aspect ratio or fractal dimension) can allow for numerical simulations (e.g. FEM, BEM, FDTD) which are more respresentative of the semiconductor material. In this manner, it is possible to evaluate, predict and engineer the final device (such as novel plasmonic solar cells and microfluidic ELISA lab-on-a-chip) by manipulating the powder to product process.

Acknowledgement

Conflict of interests

The authors report no conflict of interests. The authors alone are responsible for the content and writing of the paper.

References

Barber, V.C. & Emerson, C.J. (1979) Techniques utilizing real time stereo scanning electron microscopy in the microdissection of biological tissues. *J. Microsc.* **115**, 119–125.

Bose, S., Arokiyadoss, R., Bhargav, P.B., Ahmad, G., Mandal, S., Barua, A.K. & Mukhopadhyay, S. (2018) Modification of surface morphology of sputtered AZO films with the variation of the oxygen. *Mater. Sci. Semicond. Process.* **79**, 135–143.

Braun, C., Dake, J.M., Krill, C.E. & Birringer, R. (2018) Abnormal grain growth mediated by fractal boundary migration at the nanoscale. *Sci. Rep.* **8**, 1592.

Brown, A.T., Poon, W.C.K., Holm, C. & de Graaf, J. (2017) Ionic screening and dissociation are crucial for understanding chemical self-propulsion in polar solvents. *Soft Matter* **13**, 1200–1222.

Castro, R.H.R. & van Benthem, K. (Eds.) (2013) *Sintering: Mechanisms of Convention Nanodensification and Field Assisted Processes, Engineering Materials.* Springer, Berlin, New York.

Chen, H., Sun, Q., Tian, T., *et al.* (2020) Defects and microstructure of highly conducting Al-doped ZnO ceramics obtained via spark plasma sintering. *J. Eur. Ceram. Soc.* **40**(15), 5529–5534.

Chen, I.-W., Davenport, A. & Wang, L. (2003) Accelerated precipitate coarsening due to a concomitant secondary phase transformation. *Acta Mater.* **51**, 1691–1703.

Dallaeva, D.S., Bilalov, B.A., Gitikchiev, M.A., Kardashova, G.D., Safaraliev, G.K., Tománek, P., Škarvada, P. & Smith, S. (2012) Structural properties of Al2O3/AlN thin film prepared by magnetron sputtering of Al in HF-activated nitrogen plasma. *Thin Solid Films* **526**, 92–96.

Donkó, Z., Hartmann, P. & Kutasi, K. (2007) Effects of fast neutral particles in low-pressure gas discharges. *J. Phys.: Conf. Ser.* **71**, 012008.

Fukao, M., Ishida, M., Ohtsuka, Y. & Matsuo, H. (2000) A simple electron gun by obstructed discharge and its discharge-sustaining mechanism. Vacuum. *Sec. Int. Symp. Appl. Plasma Sci.* **59**, 358–372.

García-Cervantes, H., Gaggero-Sager, L.M., Díaz-Guerrero, D.S., Sotolongo-Costa, O. & Rodríguez-Vargas, I. (2017) Self-similar conductance patterns in graphene Cantor-like structures. *Sci. Rep.* **7**, 617.

Heilbronner, R.P. (1992) The autocorrelation function: an image processing tool for fabric analysis. *Tectonophysics* **212**, 351–370.

Huang, K., Marthinsen, K., Zhao, Q. & Logé, R.E. (2018) The double-edge effect of second-phase particles on the recrystallization behaviour and associated mechanical properties of metallic materials. *Prog. Mater Sci.* **92**, 284–359.

Ibáñez, M., Genç, A., Hasler, R., *et al.* (2019) Tuning transport properties in thermoelectric nanocomposites through inorganic ligands and heterostructured building blocks. *ACS Nano* **13**, 6572–6580.

Jafari, A., Tahani, K., Dastan, D. *et al.* (2020) Ion implantation of copper oxide thin films; statistical and experimental results. *Surf. Interf.* **18**, 100463.

Jesus, L.M., Silva, R.S. & M'Peko, J.-C. (2019) Ultrafast synthesis and sintering of materials in a single running experiment approach by using electric fields. *J. Adv. Ceram.* **8**, 265–277.

Joly-Pottuz, L., Bogner, A., Lasalle, A., Malchere, A., Thollet, G. & Deville, S. (2011) Improvements for imaging ceramics sintering in situ in ESEM. *J. Microsc.* **244**, 93–100.

Klapetek, P. (2018) *Quantitative Data Processing in Scanning Probe Microscopy: SPM Applications for Nanometrology*, 2 ed. Elsevier, Amsterdam, the Netherlands. https://www.elsevier.com/books/quantitative-data-processing-in-scanning-probe-microscopy/klapetek/978-0-12-813347-7

Knápek, A., Sýkora, J., Chlumská, J. & Sobola, D. (2017) Programmable set-up for electrochemical preparation of STM tips and ultra-sharp field emission cathodes. *Microelectr. Eng.* **173**, 42–47.

Kudryashov, M., Mochalov, L., Nezdanov, A. *et al.* (2019) A novel plasma-based method for synthesis of As-Se-Te films: impact of plasma parameters on the structure, composition, and optical properties. *Superlatt. Microstruct.* **128**, 334–341.

Lee, M., Keehm, Y. & Song, D. (2017) Quantitative analysis of resolution and smoothing effects of digital pore microstructures on numerical velocity estimation. *Geosci. J.* **21**, 431–440.

Lee, M., Park, Y., Kim, K. & Hong, J. (2020) Influence of sputtering conditions on the properties of aluminum-doped zinc oxide thin film fabricated using a facing target sputtering system. *Thin Solid Films* **703**, 137980.

Liu, H., Gao, M., Yang, B., Chen, H., Zhang, H. & Zhang, H. (2020) Characterisics of optimized Al:znO sputtering targets prepared by nanostructured powder. *Ceram. Int.* **46**, 6311–6317.

Ma, C., Lu, X., Xu, B. *et al.* (2019) Effects of sputtering parameters on photoelectric properties of AZO film for CZTS solar cell. *J. Alloys Compd.* **774**, 201–209.

Ma, Q. & Suo, Z. (1993) Precipitate drifting and coarsening caused by electromigration. *J. Appl. Phys.* **74**, 5457–5462.

Mitic, V.V., Lazovic, G., Paunovic, V., Cvetkovic, N., Jovanovic, D., Veljkovic, S., Randjelovic, B. & Vlahovic, B. (2019) Fractal frontiers in microelectronic ceramic materials. *Ceram. Int.* **45**, 9679–9685.

Monemdjou, A., Ghodsi, F.E. & Mazloom, J. (2014) The effects of surface morphology on optical and electrical properties of nanostructured AZO thin films: fractal and phase imaging analysis. *Superlatt. Microstruct.* **74**, 19–33.

Mortazavi, S.H., Jahazi, A. & Ghoranneviss, M. (2020) The effect of plasma polymerization of silicon compounds on the properties of bi-axially oriented polypropylene (BOPP). *Polym. Bull.* **77**, 1813–1828.

Mozaffari, N., Solaymani, S., Achour, A. *et al.* (2020) New insights into SnO_2/Al_2O_3, Ni/Al_2O_3, and $SnO_2/Ni/Al_2O_3$ composite films for CO adsorption: building a bridge between microstructures and adsorption properties. *J. Phys. Chem. C* **124**, 3692–3701.

Nakano, T., Saitou, Y., Ueda, M., Itamura, N. & Baba, S. (2015) Growth of target race track profile during magnetron sputtering. *J. Vac. Soc. Jpn.* **58**, 261–264.

Nečas, D. & Klapetek, P. (2012) Gwyddion: an open-source software for SPM data analysis. *Open Phys.* **10**(1).

Odziomek, K., Ushizima, D., Oberbek, P., Kurzydłowski, K.J., Puzyn, T. & Haranczyk, M. (2017) Scanning electron microscopy image representativeness: morphological data on nanoparticles. *J. Microsc.* **265**, 34–50.

Ortega, S., Ibáñez, M., Liu, Y., Zhang, Y., Kovalenko, M.V., Cadavid, D. & Cabot, A. (2017) Bottom-up engineering of thermoelectric nanomaterials and devices from solution-processed nanoparticle building blocks. *Chem. Soc. Rev.* **46**, 3510–3528.

Panjan, M. & Anders, A. (2017) Plasma potential of a moving ionization zone in DC magnetron sputtering. *J. Appl. Phys.* **121**, 063302.

Papež, N., Gajdoš, A., Sobola, D., Dallaev, R., Macků, R., Škarvada, P. & Grmela, L. (2020) Effect of gamma radiation on properties and performance of GaAs based solar cells. *Appl. Surf. Sci.* **527**, 146766.

Pelton, J.N. (2019) Space-based solar power satellite systems. In Pelton, J.N. (Ed.), *Space 2.0: Revolutionary Advances in the Space Industry.* Springer Praxis Books. Springer International Publishing, Cham, pp. 103–114.

Podor, R., Bouala, G.I.N., Ravaux, J., Lautru, J. & Clavier, N. (2019) Working with the ESEM at high temperature. *Mater. Charact.* **151**, 15–26.

Purwani, S., Nahar, J. & Twining, C. (2017) Analyzing bin-width effect on the computed entropy. Presented at the the 4th International Conference on Research, Implementation, and Education of Mathematics and Science (4th ICRIEMS). Research and Education for Developing Scientific Attitude in Sciences And Mathematics, Yogyakarta, Indonesia, p. 040008.

Raggl, S., Postler, J., Winkler, J., Strauss, G., Feist, C., Plankensteiner, A., Eidenberger-Schober, M. & Scheier, P. (2017) Correlation of target properties and plasma parameters in DC magnetron sputtering with Langmuir probe measurements. *J. Vacuum Sci. Tech. A* **35**, 061308.

Rajabi Kalvani, P., Jahangiri, A.R., Shapouri, S., Sari, A. & Jalili, Y.S. (2019) Multimode AFM analysis of aluminum-doped zinc oxide thin films sputtered under various substrate temperatures for optoelectronic applications. *Superlatt. Microstruct.* **132**, 106173.

Rajabi Kalvani, P., Shapouri, S., Jahangiri, A.R. & Jalili, Y.S. (2020) Microstructure evolution in high density AZO ceramic sputtering target fabricated via multistep sintering. *Ceram. Int.* **46**, 5983–5992.

Reyes-Gasga, J. & Becerril, N.V. (2019) Electron microscopy analysis of the thermal phase transition from hydroxyapatita to β-TCP observed in human teeth. *J. Microsc.* **276**, 89–97.

Risović, D. & Pavlović, Ž. (2013) Performance assessment of methods for estimation of fractal dimension from scanning electron microscope images: performance assessment in estimation of fractal dimension. *Scanning* **35**, 402–411.

Robertson, C. (2012) Theory and practical recommendations for autocorrelation-based image correlation spectroscopy. *J. Biomed. Opt.* **17**, 080801.

Rockstuhl, C., Fahr, S., Bittkau, K. *et al.* (2010) Comparison and optimization of randomly textured surfaces in thin-film solar cells. *Opt. Express.* **18**, A335–A342.

Röding, M., Castillo, L.a.D., Nydén, M. & Follink, B. (2016) Microstructure of a granular amorphous silica ceramic synthesized by spark plasma sintering. *J. Microsc.* **264**, 298–303.

Sagás, J.C., Pessoa, R.S. & Maciel, H.S. (2018) Langmuir probe measurements in a grid-assisted magnetron sputtering system. *Braz. J. Phys.* **48**, 61–66.

Sangwaranatee, N.W., Sangwaranatee, N., Chananonnawathorn, C. & Horprathum, M. (2018) Influence on distance between substrate and target on the properties of CuO thin film prepared by DC reactive magnetron sputtering. *Materials Today: Proceedings* **5**(6), 13900–13903.

Sari, A., Ghoranneviss, M., Henrich, H., Osman, F., Höpfl, R., Hantehzadeh, M.R. & Bolouki, N. (2004) Fabrication of a 50 keV cold cathode electron gun. *J. Plasma Fusion Res.* **6**, 735–737.

Sari, A.H., Mortazavi, S.H., Bolouki, N., Khoramabadi, M. & Ghomi, H.R. (2008) Effect of longitudinal magnetic field on a simple plasma electron source. *J. Theor. Appl. Phys. (Iranian Physical Journal)* **2**(1), 23–25.

Shakoury, R., Arman, A., Ţălu, Ş. *et al.* (2020) Optical properties, microstructure, and multifractal analyses of ZnS thin films obtained by RF magnetron sputtering. *J. Mater. Sci. Mater. Electr.* **31**, 5262–5273.

Shanmugavadivu, P. & Sivakumar, V. (2012) Fractal dimension based texture analysis of digital images. *Procedia Eng.* **38**, 2981–2986.

Shannon, C.E. (1948) A mathematical theory of communication. *Bell Syst. Tech. J.* **27**, 55.

Shapouri, S., Elahi, S.M., Dejam, L., Bagheri, Z., Ghaderi, A. & Solaymani, S. (2018) Micromorphology and optical bandgap characterization of copper oxide nanowires. *Silicon* **10**, 1911–1919.

Sun, Q., Li, G., Tian, T. *et al.* (2020) Controllable microstructure tailoring for regulating conductivity in Al-doped ZnO ceramics. *J. Eur. Ceram. Soc.* **40**, 349–354.

Sun, Q., Tian, T., Zheng, L. *et al.* (2019) Electronic active defects and local order in doped ZnO ceramics inferred from EPR and 27Al NMR investigations. *J. Eur. Ceram. Soc.* **39**, 3070–3076.

Taheriniya, S., Parhizgar, S.S. & Sari, A.H. (2018) Investigating the effect of sputtering conditions on the physical properties of aluminum thin film and the resulting alumina template. *Results Phys.* **9**, 1428–1435.

Ţălu, Ş. (2012) Mathematical methods used in monofractal and multifractal analysis for the processing of biological and medical data and images. *ABAH Bioflux* **4**(1), 1–4.

Ţălu, Ş., Bramowicz, M., Kulesza, S., Ghaderi, A., Dalouji, V., Solaymani, S., Kenari, M.F. & Ghoranneviss, M. (2016a) Fractal features and surface micromorphology of diamond nanocrystals. *J. Microsc.* **264**, 143–152.

Ţălu, Ş., Kulesza, S., Bramowicz, M., Pringle, A.M., Pearce, J.M., Murugesan, M., Venkatachalapathy, V. & Mayandi, J. (2018) Micromorphology analysis of sputtered indium tin oxide fabricated with variable ambient combinations. *Mater. Lett.* **220**, 169–171.

Ţălu, Ş., Morozov, I.A. & Yadav, R.P. (2019) Multifractal analysis of sputtered indium tin oxide thin film surfaces. *Appl. Surf. Sci.* **484**, 892–898.

Ţălu, Ş., (2015) *Micro and Nanoscale Characterization of Three Dimensional Surfaces. Basics and Applications*, 1st ed. Napoca Star Publishing House, Cluj-Napoca, Romania.

Ţălu, Ş., Solaymani, S., Bramowicz, M., Kulesza, S., Ghaderi, A., Shahpouri, S. & Elahi, S.M. (2016b) Effect of electric field direction and substrate roughness on three-dimensional self-assembly growth of copper oxide nanowires. *J. Mater. Sci. Mater. Electr.* **27**, 9272–9277.

Tavakoli, M. & Jalili, Y.S. (2014) One-dimensional Fibonacci fractal photonic crystals and their optical characteristics. *J. Theor. Appl. Phys.* **8**, 113.

Thiruvalluvan, T.M.V.M., Natarajan, V., Manimuthu, V., Valanarasu, S., Anandan, P. & Arivanandhan, M. (2018) Effects of Al composition on the secondary phase formation and thermoelectric properties of Zn 1-x Al x O nanocrystals. *J. Phys. Chem. Solids* **122**, 162–166.

van Veen, E., Tomadin, A., Polini, M., Katsnelson, M.I & Yuan, S. (2017) Optical conductivity of a quantum electron gas in a Sierpinski carpet. *Phys. Rev. B 96.*

Vermolen, E.C.M., Kuijk, A., Filion, L.C., Hermes, M., Thijssen, J.H.J., Dijkstra, M. & van Blaaderen, A. (2009) Fabrication of large binary colloidal crystals with a NaCl structure. *Proc. Natl. Acad. Sci.* **106**, 16063–16067.

Wu, J., Wang, Z., Chen, F., Shen, Q. & Zhang, L. (2019) Chemical evolution of target surfaces during RF magnetron sputtering and its effect on the performance of TCO films. *Appl. Surf. Sci.* **493**, 665–672.

Wu, M.-W., Liu, D.-S. & Su, Y.-H. (2012) The densification, microstructure, and electrical properties of aluminum-doped zinc oxide sputtering target for transparent conductive oxide film. *J. Eur. Ceram. Soc.* **32**, 3265–3275.

Yan, S., Adegbule, A. & Kibbey, T.C.G. (2019) A boosted decision tree approach to shadow detection in scanning electron microscope (SEM) images for machine vision applications. *Ultramicroscopy* **197**, 122–128.

Zhang, Z., Duan, X., Qiu, B., Yang, Z., Cai, D., He, P., Jia, D. & Zhou, Y. (2019) Preparation and anisotropic properties of textured structural ceramics: a review. *J. Adv. Ceram.* **8**, 289–332.

Zhao, Y., Chen, B., Miner, A. & Priya, S. (2014) Low thermal conductivity of Al-doped ZnO with layered and correlated grains. *RSC Adv.* **4**, 18370.